PCCP
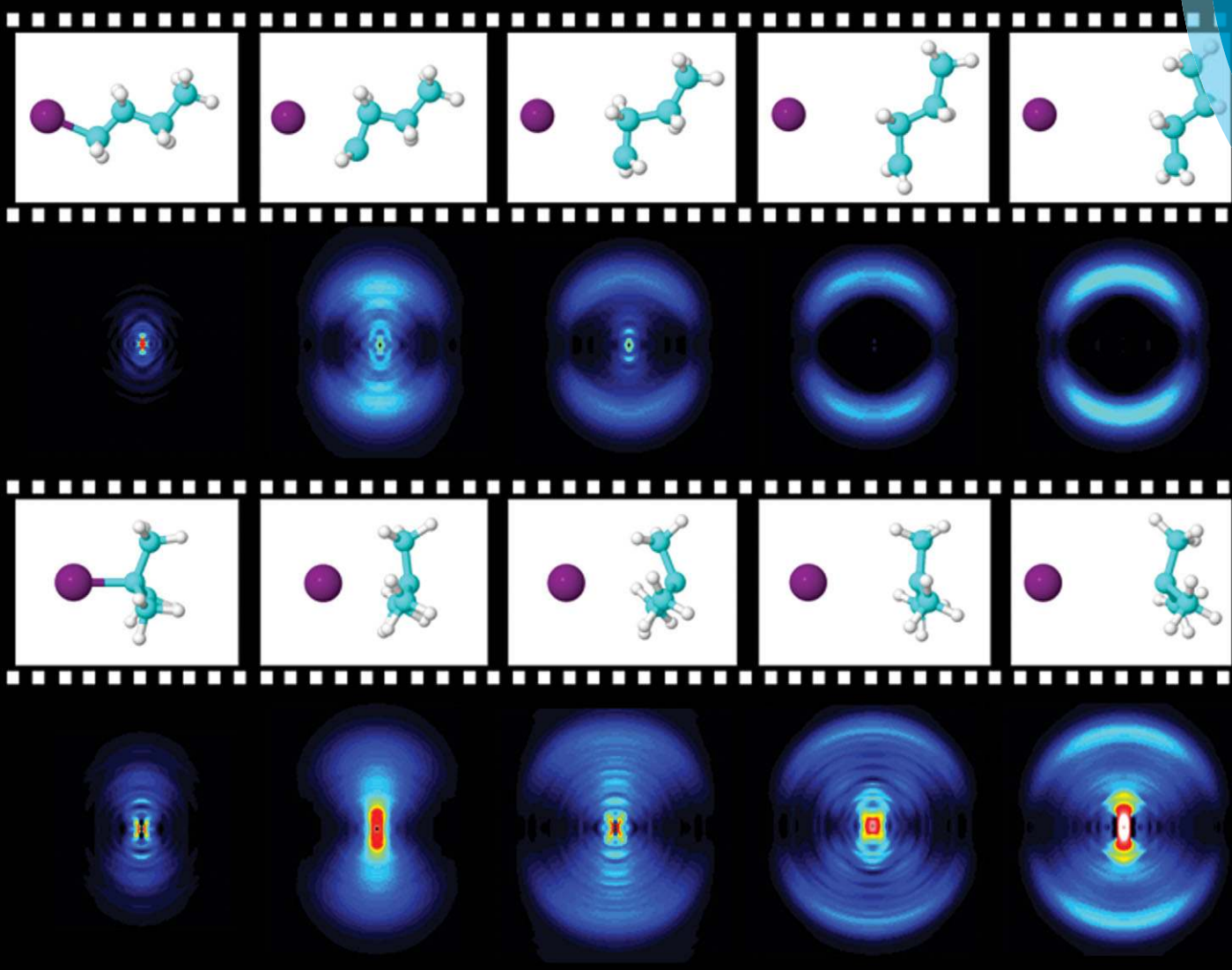
Physical Chemistry Chemical Physics

www.rsc.org/pccp

ROYAL SOCIETY
OF CHEMISTRY

PAPER
Luis Bañares, Ahmed H. Zewail *et al.*
Structural dynamics effects on the ultrafast chemical bond cleavage of a
photodissociation reaction

Structural dynamics effects on the ultrafast chemical bond cleavage of a photodissociation reaction†

María E. Corrales,[a] Vincent Loriot,[ab] Garikoitz Balerdi,[a] Jesús González-Vázquez,[ab] Rebeca de Nalda,[b] Luis Bañares*[a] and Ahmed H. Zewail*[c]

The correlation between chemical structure and dynamics has been explored in a series of molecules with increasing structural complexity in order to investigate its influence on bond cleavage reaction times in a photodissociation event. Femtosecond time-resolved velocity map imaging spectroscopy reveals specificity of the ultrafast carbon–iodine (C–I) bond breakage for a series of linear (unbranched) and branched alkyl iodides, due to the interplay between the pure reaction coordinate and the rest of the degrees of freedom associated with the molecular structure details. Full-dimension time-resolved dynamics calculations support the experimental evidence and provide insight into the structure–dynamics relationship to understand structural control on time-resolved reactivity.

Introduction

The relationship between static molecular structure and chemical reactivity has been a cornerstone in organic chemistry over the years. For instance, electrophilic substitution in aromatic molecules has been extensively employed to tune chemical reactivity in specific chemical attack sites (*ortho*, *meta* and *para*) and to define different synthesis routes.[1] However, the relation between the dynamics associated with key structural changes in the molecule and the outcome of a chemical reaction has been much less explored. In a series of papers, Stolow and co-workers and Soep and co-workers studied substituent effects on the photochemical dynamics at conical intersections in a series of molecules like substituted benzenes,[2] ethylenes,[3,4] cyclopentadienes[5,6] and α,β-enones[7] by using ultrafast photoelectron spectroscopy. The key point in those studies was to discern the role of electronic structure, density of states and floppiness or rigidity of the molecular structure in the

electronically non-adiabatic dynamics by systematic chemical substitution. In a way, the aim was to find an equivalent of the "Polanyi rules"[8] for excited state polyatomic dynamics, in such a way that specific vibrational dynamics at conical intersections would be as important to dynamics as are the topographical features of the conical intersections themselves.[5]

In the present work, the aim is to demonstrate the role of the dynamics associated with key structural changes in the molecule to influence reactivity in terms of reaction times in photodissociation. In a series of molecules containing the same reaction coordinate but different extended structures, we show a correlation between the reaction (bond cleavage) time and the dynamics associated with the chemical structure of the molecule. Specifically, we have examined a series of R–I molecules sharing the same carbon–iodine (C–I) reaction coordinate but with varying alkyl radical chain R, which makes the molecule either linear (unbranched) or branched. The linear molecules studied are CH_3I, C_2H_5I, $n\text{-}C_3H_7I$ and $n\text{-}C_4H_9I$, and those branched are $i\text{-}C_3H_7I$ and $t\text{-}C_4H_9I$ (chemical structures are shown in Fig. 2).

Time-resolved measurements (reaction times for the C–I bond cleavage in the first absorption band of the molecules) have been carried out by means of femtosecond velocity map imaging spectroscopy,[9,10] which provides in addition the angular and velocity distributions of the fragments as a function of time. This series of molecules shares the same electronic structure upon absorption of a UV femtosecond laser pulse at 268 nm and a common C–I dissociation mediated by a conical intersection between two optically active electronically excited states, the $^1Q_1$ and $^3Q_0$ states, in the so-called A-band[10,11] (see Fig. 1).

[a] *Departamento de Química Física, Facultad de Ciencias Químicas (Unidad Asociada I+D+i al CSIC), Universidad Complutense de Madrid, 28040 Madrid, Spain. E-mail: lbanares@ucm.es; Fax: +34 913944135; Tel: +34 913944228*

[b] *Instituto de Química Física Rocasolano, CSIC, C/ Serrano, 119, 28006 Madrid, Spain*

[c] *Physical Biology Center for Ultrafast Science & Technology, Arthur Amos Noyes Laboratory of Chemical Physics, California Institute of Technology, Pasadena, CA 91125, USA. E-mail: zewail@caltech.edu*

† Electronic supplementary information (ESI) available: Transients for the photodissociation reaction yielding spin–orbit excited $I^*(^2P_{1/2})$ for the different alkyl iodides studied. Potential energy curves calculated at the CASPT2 level of theory for all molecules studied. Movies of specific on-the-fly trajectories for all the molecules in both the linear and branched series. See DOI: 10.1039/c3cp54677b
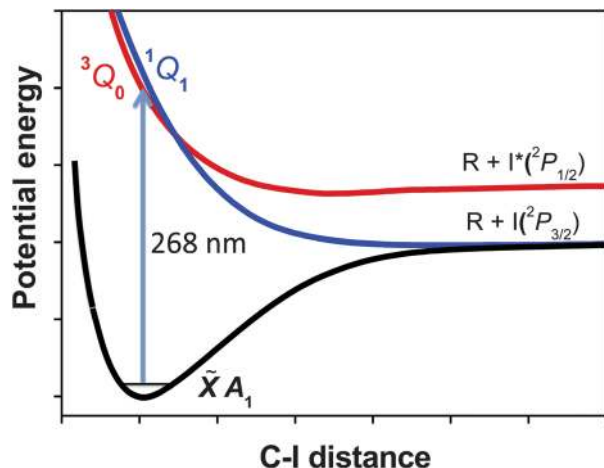
Fig. 1 Schematic representation of the relevant potential energy curves along the C–I distance for the electronic states involved in the A-band photodissociation of the RI alkyl iodides studied in this work. After one-photon 268 nm excitation the $^3Q_0$ state, which correlates with R + I*($^2P_{1/2}$), is accessed. A non-adiabatic crossing with the $^1Q_1$ state allows production of R + I($^2P_{3/2}$).

The clocking of the reactions is carried out by a time-delayed femtosecond laser pulse, which can resonantly multiphoton ionize the iodine fragments both in the ground and spin–orbit excited states, I($^2P_{3/2}$) and I*($^2P_{1/2}$), respectively.

Methodology

Femtosecond pump–probe velocity map imaging spectroscopy has been used to measure photodissociation reaction times of the series of molecules depicted in Fig. 2. In all cases, the excitation to the maximum of the A-band is carried out by a femtosecond pump laser centered at 268 nm (1 μJ per pulse) corresponding to the third harmonic of a fraction of the output of an amplified femtosecond laser system, 3.5 mJ pulses of 50 fs duration at 1 kHz repetition rate with a central wavelength of 804 nm. The probe laser pulse, centered at 304.5 nm to ionize the iodine fragment atoms by (2+1) resonance-enhanced multiphoton ionization (REMPI) (I($^2P_{3/2}$) through the $6p^4D_{7/2}$ and $6p^4D_{1/2}$ states, and I*($^2P_{1/2}$) through the $6p^4P_{3/2}$ and $6p^4D_{1/2}$ states) and with typically 5 μJ per pulse, is generated in an optical parametric amplifier (OPA) pumped by a fraction of the fundamental laser output after frequency quadrupling the 1333.8 nm signal pulse. Given the bandwidth of the probe laser, both I($^2P_{3/2}$) and I*($^2P_{1/2}$) fragments can be resonantly ionized at 304.5 nm. The delay between the pump and probe pulses is controlled by a motorized delay stage placed at the probe laser arm that allows time steps as low as 1 fs. The two laser beams are focused with a 25 cm focal length lens onto a pulsed molecular beam inside a differentially pumped vacuum chamber. The molecular beam is generated by expansion of the molecule of interest at 0 °C or room temperature, seeded in He, at a total pressure of 1.5–2 bars, through a 0.5 mm diameter nozzle, 1 kHz cantilever piezoelectric pulsed valve. A 1 mm diameter skimmer separates the expansion and ionization
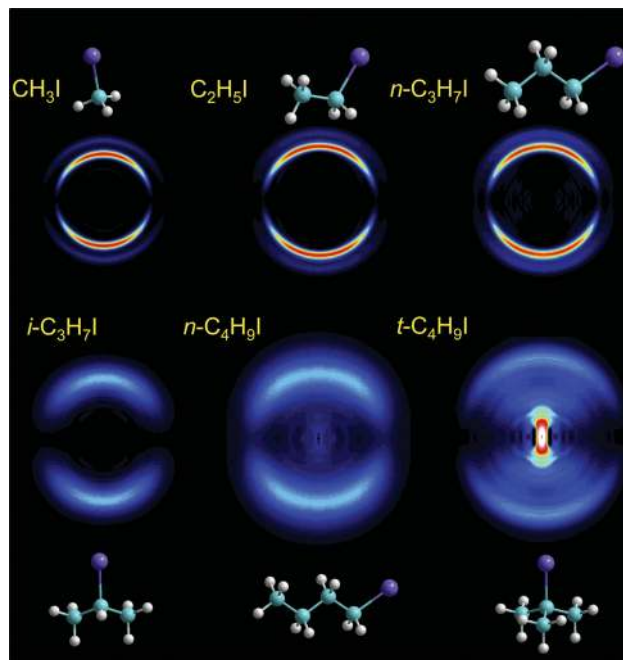

Fig. 2 Abel inverted iodine images measured in femtosecond pump–probe velocity map imaging experiments for the series of alkyl iodide molecules. The pump laser pulse (268 nm) excites the molecules to the maximum of the first absorption A-band. The probe laser pulse (304.5 nm) ionizes the iodine fragments by (2+1) REMPI both in the ground ($^2P_{3/2}$) and spin–orbit excited ($^2P_{1/2}$) states. The time delay between the pump and probe pulses is 1 ps. In the images, the radius is proportional to the velocity of the fragments. The linear polarization of the lasers is vertical.

chambers, where the molecular beam interacts with the laser pulses. Generated ions are extracted by a set of electrostatic lenses working in velocity mapping configuration,[9] and mass separated in a 50 cm field-free region time-of-flight (TOF) mass spectrometer. Ion spheres are projected onto a detector consisting of a dual microchannel plate (MCP) in Chevron configuration coupled to a phosphor screen and a Peltier-cooled 12-bit charge-coupled device camera. The front MCP plate is gain-gated in order to achieve mass selection. Kinetic energy-radius calibration is done by measuring resonantly ionized $CH_3(\nu = 0)$ fragments at 333.45 nm after photodissociation of CH_3I at 268 nm, taking advantage of the well known kinetic energy release (KER) for both I*($^2P_{1/2}$) and I($^2P_{3/2}$) yielding channels. Ion images are Abel inverted using the polar basis set expansion (pBASEX)[12] method and a Levenberg–Marquardt squared residuals minimization algorithm[13] is used for fits to the data. The instrument temporal response time, considered as the temporal cross-correlation of the pump and probe pulses, was measured by 1+1′ multiphoton ionization of Xe, obtaining a value of 150 fs. This same method was used to determine time-zero *in situ*.

Ab initio CASPT2 electronic structure calculations of the ground and excited potential energy curves including spin–orbit have been carried out for all the molecules studied. In these calculations, the potential energy was evaluated as a function of the C–I distance and at each point the geometry of the molecule was optimized at the CAS(6,4)/ANO-L level of

theory along with State Average (SA) wavefunctions. The energy was corrected with perturbation theory in its multireference form CASPT2. The basis set ANO-L was contracted to be equivalent to a triple zeta polarized one and the active space includes the orbitals of the two lone pairs of the iodine and the bonding and antibonding orbitals of C–I. The Hamiltonian was modified using the Douglas–Kroll approximation to consider relativistic effects. The geometries were optimized and their frequencies calculated at the single-state CASPT2 level of theory, for the ground electronic state, with analytical gradients as implemented in the MOLPRO package.[14] In this case, we include an SA of three singlet states in a SA3-CAS(6,4) calculation. In order to describe correctly the adiabatic energies, singlet point calculations were performed at this geometry including the previous singlet SA3-CAS(6,4) and another SA3-CAS(6,4) for the triplet states, and the energies were recalculated using MS-CASPT2,[15] independently of singlet and triplet states. Finally, spin–orbit coupling was taken into account using the AMFI approximation and the corresponding singlet–triplet Hamiltonian was diagonalized. These single point calculations were done using MOLCAS[16] and they reveal that the dissociation energies, the shape of the relevant potential energy curves and the position of the $^3Q_0/^1Q_1$ conical intersection are similar for the different molecules studied (see Table 1).

On-the-fly adiabatic full-dimension classical trajectory calculations have been run using a modified version of SHARC,[21] where the surface hopping algorithm was removed, but spin–orbit coupling was considered in the evaluation of the gradients. The on-the-fly trajectory calculations use a smaller basis set of Stoll and co-workers for the valence electrons of C and I, with its corresponding pseudo-potentials for the inner electrons, and a DZP for the H-atom (CAS/ECP method). The trajectories are started at the Franck–Condon region of the $^3Q_0$ surface and once at the conical intersection with the $^1Q_1$ surface a crossing with unity probability is forced, so that the trajectories end in the $I(^2P_{3/2})$ + CH_3 asymptote. About 10 trajectories sampling different initial conditions according to a Wigner distribution have been run for each molecule. Due to the lack of dynamic electronic correlation in the CASSCF method, the calculated dissociation energies are significantly smaller in comparison with the CASPT2 and experimental values.

However, it is observed that the available energy is similar for all molecules, and thus this methodology should be able to give at least a qualitative picture of the energy flux along the reaction coordinate as the dissociation proceeds for the different molecules. An end point for the trajectories has been fixed at 4.8 Å beyond the equilibrium distance as the distance where the fragments can be considered free, and has been chosen for global agreement with experimental reaction times. In order to calculate the reaction times, a Gaussian envelope was assigned to the distance between the I-atom and the center of mass of the radical group for every trajectory. In the asymptotic region (chosen to be 4.8 Å from the equilibrium geometry), the time evolution of the sum of Gaussian envelopes was integrated describing the population beyond the probe region. Finally, the reaction time was obtained by fitting this population to a sigmoidal function.

Results and discussion

Fig. 2 depicts Abel inverted iodine ion images obtained at a long delay time between the excitation and ionization laser pulses, when the reaction has already finished and the radical R and the I-atom can be considered as free fragments.

As can be appreciated, there are significant changes in the characteristic rings representing specific reaction channels for the series of molecules. However, the anisotropy associated with the measured iodine fragment angular distribution is very similar in all cases, characteristic of a parallel transition and a similar non-adiabatic photodissociation mechanism.[4] Two sharp rings are clearly observed for the smaller molecules (CH_3I, C_2H_5I and n-C_3H_7I), indicating narrow velocity distributions of the iodine fragment. However, this picture changes considerably for the larger molecules (i-C_3H_7I, n-C_4H_9I and t-C_4H_9I), where only one fuzzy broad ring is observed. Measurements of the quantum yields of the reaction by time-resolved photoelectron imaging spectroscopy‡ reveal that the two channels yielding $I(^2P_{3/2})$ and $I^*(^2P_{1/2})$ are present for all the molecules, although with varying branching ratios. In particular, for the branched molecules, the amount of $I^*(^2P_{1/2})$ generated in the reaction is minor. Thus, the changes observed in the iodine images are related mainly to the different energy release of the possible reaction channels, which are dependent on the molecule.

Indeed, important information that can be extracted from the images shown in Fig. 2 is the fraction of the total energy available after excitation that appears as internal energy (both rotational and vibrational) of the R fragment. Angular integration of the images provides the total translational energy distributions (TEDs) depicted in Fig. 3, from where the fraction values reported in Table 2 can be obtained. It is clear that there is a tendency for the internal energy of the R fragment to

Table 1 Dissociation energy (D_0) of the alkyl iodides studied in this work calculated at the CASPT2 level of theory compared with the available experimental data (D_0^{exp}). The C–I distance of the $^3Q_0/^1Q_1$ non-adiabatic crossing (R_{CI}) is also included

	D_0/eV	D_0^{exp}/eV	R_{CI}/Å
Linear			
CH_3I	2.58	2.41 [17]	2.34
C_2H_5I	2.62	2.35 [18]	2.31
n-C_3H_7I	2.69	2.36 [19]	2.31
n-C_4H_9I	2.72	2.34 [20]	2.31
Branched			
i-C_3H_7I	2.66	2.30 [19]	2.32
t-C_4H_9I	2.75	2.21 [20]	2.28

‡ We have measured time resolved photoelectron images by resonant multiphoton ionization of the iodine atoms. Deconvolution of the photoelectron translational energy distributions derived from the images using a multidimensional least-square fitting procedure yields the quantum yields for production of $I(^2P_{3/2})$ and $I^*(^2P_{1/2})$.

8814 | *Phys. Chem. Chem. Phys.*, 2014, **16**, 8812–8818
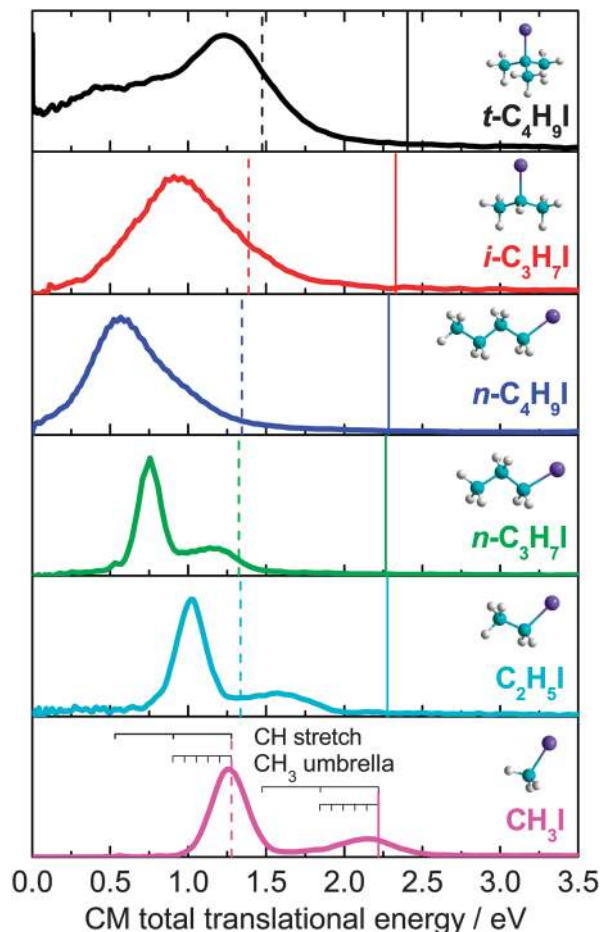
This journal is © the Owner Societies 2014

Fig. 3 Center-of-mass (CM) total translational energy distributions of the different alkyl iodides studied obtained from the images shown in Fig. 2. The dashed and solid vertical lines correspond to the available energy for the I($^2P_{3/2}$) and I*($^2P_{1/2}$) channels, respectively, according to the known dissociation energies of the different molecules. The combs at the bottom panel indicate the vibrational states corresponding to the CH stretch and umbrella modes of the CH$_3$ co-fragment.

Table 2 Fraction of the available energy appearing as internal energy of the radical R, $f_{int} = E_{int}/E_{av}$ (where E_{int} is the internal energy of R and E_{av} is the available energy calculated as the difference between the energy of the excitation photon and the dissociation energy of the molecule, after dissociation of the series of molecules at 268 nm. Uncertainties for the f_{int} values are around 10%. I and I* stand for the reaction channels yielding spin–orbit ground and excited state iodine atoms, I($^2P_{3/2}$) and I*($^2P_{1/2}$), respectively. For the branched molecules, the quantum yield for production of I*($^2P_{1/2}$) is less than 0.2. Theoretical values f_{int}th obtained from on-the-fly trajectory calculations based on the CASSCF level of theory for the channel yielding I($^2P_{3/2}$) are also included

	f_{int}(I*)	f_{int}(I)	f_{int}th(I)
Linear			
CH$_3$I	0.09	0.12	0.20
C$_2$H$_5$I	0.27	0.32	0.53
n-C$_3$H$_7$I	0.45	0.53	0.67
n-C$_4$H$_9$I	0.57	0.60	0.68
Branched			
i-C$_3$H$_7$I	—	0.56	0.63
t-C$_4$H$_9$I	—	0.49	0.60

increase as we move from the smaller to the larger linear molecules.[11] As the vibrational degrees of freedom and size of the linear radical R increase, more energy is released as internal energy and less as translational energy of the fragments. In fact, it is for the I($^2P_{3/2}$) channel of the reaction where this effect is stronger and explains why the two channels overlap for the largest linear molecule. This result also explains why the rings become broader and fuzzy as the size and complexity of R increase. A surprising different behavior is observed, however, for the branched molecules. In that case, this quantity decreases (t-C$_4$H$_9$I) or stabilizes (i-C$_3$H$_7$I) with respect to their linear counterparts. This implies that the amount of the total energy that is released as translational energy of the fragments increases for the branched molecules as compared with the corresponding linear ones or, in other words, the energy flux into the internal degrees of freedom of the branched radical is less effective. As we will show below, this has important repercussions on the observed reaction times.

These results on the fraction of available energy appearing as internal energy of the radical R for the series of molecules studied in this work are in good agreement with previous data obtained in nanosecond laser experiments along the years.[11,20,22–26]

The C–I bond cleavage (clocking) times in the series of molecules are measured by monitoring the evolution of the intensity of the iodine fragment rings in the images as a function of time. The resulting transients for the reaction channel yielding the ground state I($^2P_{3/2}$) are depicted in Fig. 4. Similar transients have been measured for the reaction channel yielding spin–orbit excited I*($^2P_{1/2}$) (see ESI†). Table 3 summarizes all the clocking times measured. Reaction times for both channels, I($^2P_{3/2}$) or I*($^2P_{1/2}$), steadily increase with increasing R radical size. The exception to this trend is for the branched molecules (i-C$_3$H$_7$I and t-C$_4$H$_9$I) when compared to the corresponding linear ones (n-C$_3$H$_7$I and n-C$_4$H$_9$I), which show a shorter reaction time by about 13%. Thus, the branched molecules, showing a smaller fraction of the available energy released as internal energy of the radical fragment (see above), also show a faster reaction time.

Reaction time and energy release appear to be strongly correlated for the series of linear and branched molecules. In order to rationalize this correlation, we have used a simple 1D classical model[27] in which the reaction time, τ, can be expressed as

$$\tau = \mu^{1/2} \int_{R_i}^{R_f} \frac{dR}{\sqrt{2(E - V(R))}} \qquad (1)$$

where R_i and R_f are the initial and final separations between the iodine atom and its co-fragment, E is the total energy available for dissociation after absorption of a 268 nm photon, μ is the reduced mass of the molecule and $V(R)$ is the potential energy of the molecule as a function of the C–I coordinate.

Assuming that $V(R)$§ is similar for all the molecules studied irrespective of the radical R (a notion that has been confirmed

---

§ As in ref. 27, an exponential form has been assumed for the potential energy curve $V(R) = E \exp(-(R - R_0)/L)$, common to all the molecules studied.
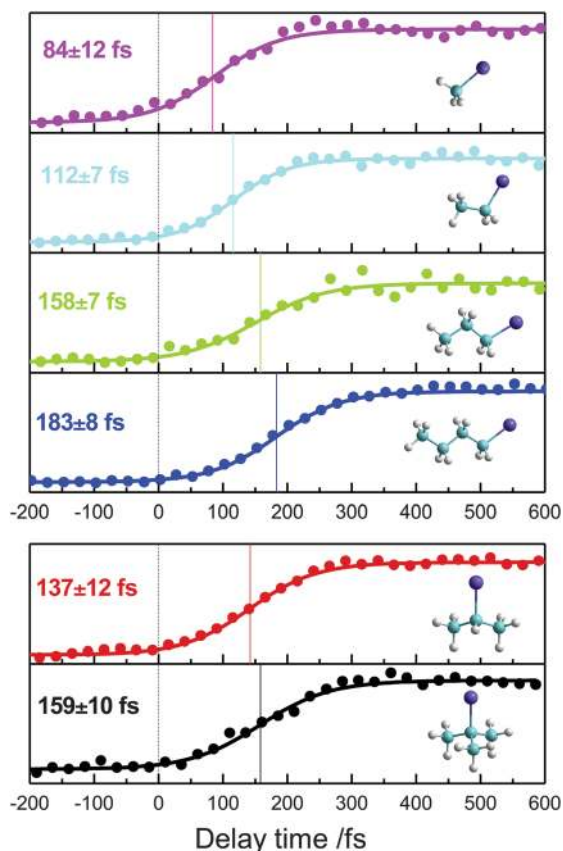
Fig. 4 Transients measured for the series of (linear and branched) alkyl iodide molecules for the channel of the reaction yielding ground state iodine $^2P_{3/2}$ atoms. Similar transients were measured for the channel yielding spin–orbit excited iodine $^2P_{1/2}$ atoms for the linear molecules (see ESI†). The reaction (clocking) times are referred to the time zero found *in situ* by measuring the 1+1′ ionization signal in Xe. Time zero is indicated in each panel by means of a vertical dashed line. The reaction time is defined as the time between time zero and the time corresponding to the middle of the rise of the transient (indicated by vertical lines in each panel). The reaction times obtained as a mean value of several measurements along with the error bar reflecting the standard deviation are indicated in each panel.

Table 3 Reaction times (τ) for the photodissociation of the linear and branched molecules studied in this work. I* and I stand for the channels yielding I*($^2P_{1/2}$) and I($^2P_{3/2}$), respectively. For the branched molecules, the quantum yield for production of I*($^2P_{1/2}$) is less than 0.2. Theoretical values (τth) obtained from on-the-fly trajectory calculations based on the CASSCF level of theory for the channel yielding I($^2P_{3/2}$) are also included

	τ(I*)/fs	τ(I)/fs	τth(I)/fs
Linear			
CH_3I	94 ± 6	84 ± 13	76
C_2H_5I	129 ± 4	112 ± 7	117
$n\text{-}C_3H_7I$	166 ± 4	158 ± 7	149
$n\text{-}C_4H_9I$	193 ± 7	183 ± 8	183
Non-linear			
$i\text{-}C_3H_7I$	—	137 ± 12	143
$t\text{-}C_4H_9I$	—	159 ± 10	160

by high level *ab initio* calculations – see ESI†), then it can be found that $\tau \propto (\mu/2E')^{1/2}$, where the new energy variable E' is introduced to account for the energy release in the internal

degrees of freedom of the fragments during the dissociation process for the series of molecules. Thus, the energy variable E' accounts for the difference between the total available energy, E_{av}, and the internal energy of the radical R, $E' = E_{av} - E_{int} = E_{av}(1 - f_{int})$, where the $f_{int} = E_{int}/E_{av}$ values are taken from Table 2.

Fig. 5 shows how the reaction times of the linear molecules for the channel yielding I*($^2P_{1/2}$) does indeed depend linearly on $(\mu/2E')^{1/2}$. The important consequence of this result is that time-resolved C–I bond breakage in the linear molecules is fully accounted for by the radical size and the energy release into the radical fragment, according to the model.

Interestingly, the same behavior is found for the linear and branched molecules for the reaction channel yielding I($^2P_{3/2}$), as depicted in the bottom panel of Fig. 5. This result for the branched molecules is to a good extent expected, considering the reduction in the energy release into the internal degrees of freedom of the branched radicals, in parallel with the reduction of reaction times, when compared to the linear molecules of the same size. Therefore, the reaction times of the series of linear and branched molecules studied can be predicted simply by considering the molecular mass and the proportion of the available energy released into internal degrees of freedom of the radical R. However, the energy release into the fragments for the series of molecules depends indeed on the structural dynamics during the bond-breaking process.
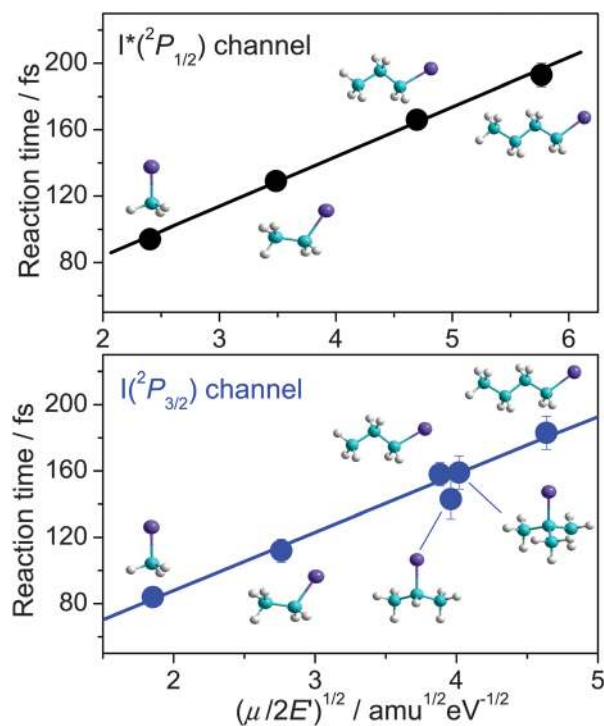

Fig. 5 Representation of the reaction time *versus* $(\mu/2E')^{1/2}$, where μ is the reduced mass of the molecule and E' is a modified energy variable which considers the available energy after subtraction of the amount of energy channelled into internal modes of the radical R for each molecule. (Top) Linear molecules dissociating into I*($^2P_{1/2}$). (Bottom) Linear and branched molecules dissociating into I($^2P_{3/2}$). Straight lines are linear fits to the data.

8816 | *Phys. Chem. Chem. Phys.*, 2014, **16**, 8812–8818

This journal is © the Owner Societies 2014

To what extent the dynamics associated with the structure of the molecule is conditioning the reaction times is a question that we would like to address in view of the above results. For this purpose, on-the-fly adiabatic full-dimension classical trajectory calculations have been run at the *ab initio* complete active space self-consistent field (CASSCF) level of theory. The theoretical reaction times for the dissociation yielding ground-state iodine atoms are listed in Table 3 along with the experimental values. A good agreement is found between theory and experiment for the reaction times. The agreement is qualitative with respect to the fraction of available energy channelled into internal degrees of freedom of the R fragment (see Table 2). The classical trajectories are then useful to gain insight into the dynamical aspects associated with the chemical structure, which condition the rate of the reaction.

Fig. 6 shows snapshots corresponding to selected trajectories for the largest linear and branched molecules, n-C_4H_9I and t-C_4H_9I, respectively, where the effects are seen to be most prominent. As can be seen, distinct early-stage dynamical features during the C–I bond cleavage are involved for the two molecules. For the linear n-C_4H_9I molecule, the early steps of the bond-breaking process are dominated by a large amplitude rotational motion of the linear radical R. During rotation, the radical behaves as a rigid chain and its associated vibrational motions play a relatively minor role in the dynamics. Energy flux into rotation of the radical fragment is efficient, reducing the amount of energy released as translational energy and making the rate of the reaction lower. For this linear molecule, only the C–I dimension plays a major role in the dissociation dynamics. This kind of structural dynamics is dominant for the dissociation of the series of linear molecules in both channels of the reaction.

The picture is completely different for t-C_4H_9I where, the initial steps of the cleavage are dominated by a prominent umbrella-like bending motion involving the branched structure of the radical fragment. In this case, no torque can be exerted on the radical and energy transfer into the radical is less efficient, producing an increase of the amount of energy released as translational energy and thus a faster reaction rate. Now the reaction coordinate cannot be just considered as the single dimension C–I motion, but as a multidimensional motion in which the flux of energy in key vibrational degrees of freedom, in particular, the umbrella mode of the branched radical, plays a significant role.[24] With these considerations, i-C_3H_7I represents an intermediate case between a pure linear molecule and a pure branched molecule. Movies of specific on-the-fly trajectories for all the molecules in both the linear and branched series supporting these mechanisms are available as ESI.†

Conclusions

The influence on the rate of a photodissociation reaction (C–I cleavage time) by the dynamics associated with the chemical structure that has been shown in the series of alkyl iodide molecules studied in this work can be considered as a general case in reaction dynamics. We have demonstrated that energy flux in the internal degrees of freedom of the molecule, both rotation and vibration, is one of the key factors governing reaction rates and its full exploitation will be the aim of future research for other series of molecules where structural dynamics plays a fundamental role in chemical reactivity.

Acknowledgements

Fig. 6 Snapshots corresponding to selected on-the-fly trajectories for the dissociation of the linear n-C_4H_9I and branched t-C_4H_9I molecules (see the text for more details). In each frame, the time and ΔR, *i.e.* the increase of the distance between the iodine atom and the center-of-mass of the radical fragment, are indicated. At time zero, $\Delta R = 0$, and the C–I distance corresponds to the equilibrium distance of the molecule.

Notes and references

1 J. Clayden, N. Greeves and S. Warren, *Organic Chemistry*, Oxford University Press, Oxford, 2nd edn, 2012.

2 S.-H. Lee, K.-C. Tang, I.-C. Chen, M. Schmitt, J. P. Shaffer, T. Schultz, J. G. Underwood, M. Z. Zgierski and A. Stolow, *J. Phys. Chem. A*, 2002, **106**, 8979.

3 J. M. Mestdagh, J. P. Visticot, M. Elhanine and B. Soep, *J. Chem. Phys.*, 2000, **113**, 237.

4 S. Sorgues, J. M. Mestdagh, J. P. Visticot and B. Soep, *Phys. Rev. Lett.*, 2003, **91**, 103001.

5 O. Schalk, A. E. Bogulavski and A. Stolow, *J. Phys. Chem. A*, 2010, **114**, 4058.

6 M. A. Lee, J. D. Coe, S. Ullrich, M.-L. Ho, S.-J. Lee, B.-M. Cheng, M. Z. Zgierski, I.-C. Chen, T. J. Martinez and A. Stolow, *J. Phys. Chem. A*, 2007, **111**, 11948.

7 G. Wu, A. Bogulavski, O. Schalk, M. S. Schuuman and A. Stolow, *J. Chem. Phys.*, 2011, **135**, 164309.

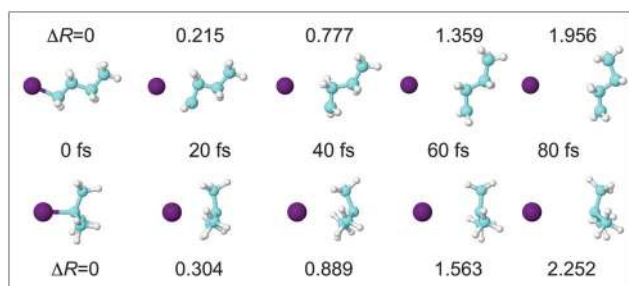8 R. D. Levine, *Molecular Reaction Dynamics*, Cambridge University Press, Cambridge, 2005.

This journal is © the Owner Societies 2014

Phys. Chem. Chem. Phys., 2014, **16**, 8812–8818 | 8817

9 A. T. J. B. Eppink and D. H. Parker, *Rev. Sci. Instrum.*, 1997, **68**, 3477.

10 R. de Nalda, J. Durá, A. García-Vela, J. G. Izquierdo, J. González-Vázquez and L. Bañares, *J. Chem. Phys.*, 2008, **128**, 244309.

11 S. J. Riley and K. R. Wilson, *Faraday Discuss.*, 1972, **53**, 132.

12 G. A. García, L. Nahon and I. Powis, *Rev. Sci. Instrum.*, 2004, **75**, 4989.

13 G. Gitzinger, M. E. Corrales, V. Loriot, R. de Nalda and L. Bañares, *J. Chem. Phys.*, 2012, **136**, 074303.

14 H.-J. Werner, P. J. Knowles, R. Lindh, F. R. Manby and M. Schütz, *et al.*, MOLPRO, Version 2009.1.

15 J. Finley, P.-Å. Malmqvist, B. O. Roos and L. Serrano-Andrés, *Chem. Phys. Lett.*, 1998, **288**, 299–306.

16 F. Aquilante, L. De Vico, N. Ferré, G. Ghigo, P.-Å. Malmqvist, P. Neogrády, T. B. Pedersen, M. Pitoňák, M. Reiher, B. O. Roos, L. Serrano-Andrés, M. Urban, V. Veryazov and R. Lindh, *J. Comput. Chem.*, 2010, **31**, 224.

17 A. T. J. B. Eppink and D. H. Parker, *J. Chem. Phys.*, 1999, **110**, 832.

18 C. Paterson, F. Godwin and P. Gorry, *Mol. Phys.*, 1987, **60**, 729.

19 F. Godwin, C. Paterson and P. Gorry, *Mol. Phys.*, 1987, **61**, 827.

20 Y. S. Kim, W. K. Kang, D. Kim and K. Jung, *J. Phys. Chem. A*, 1997, **101**, 7576.

21 M. Richter, P. Marquetand, J. González-Vázquez, I. Solá and L. González, *J. Chem. Theory Comput.*, 2011, **7**, 1253.

22 M. O. Hale, G. E. Galica, S. G. Glogover and J. L. Kinsey, *J. Phys. Chem.*, 1986, **90**, 4997.

23 Q. Zhu, J. Cao, Y. Wen, J. Zhang, X. Zhong, Y. Huang, W. Fang and X. Wu, *Chem. Phys. Lett.*, 1988, **144**, 486.

24 D. L. Phillips, B. A. Lawrence and J. J. Valentini, *J. Phys. Chem.*, 1991, **95**, 9085.

25 S. Uma and P. K. Das, *J. Chem. Phys.*, 1996, **104**, 4470.

26 V. A. Shubert, M. Rednic and S. T. Pratt, *J. Chem. Phys.*, 2009, **130**, 134306.

27 Q. Liu and A. H. Zewail, *J. Phys. Chem.*, 1993, **97**, 2209.